Structural Dynamics of an ELM-11 Framework Transformation Accompanied with Double-Step CO$_2$ Gate Sorption: An NMR Spin Relaxation Study

Kazuki Ohazama [1], Takahiro Ueda [2,3,*], Kazuki Ukai [2], Manami Ichikawa [1], Hyuma Masu [4], Hiroshi Kajiro [5] and Hirofumi Kanoh [1,*]

[1] Department of Chemistry, Chiba University, 1-33 Yayoi-cho, Inage-ku, Chiba 263-8522, Japan; kaz11281991@gmail.com (K.O.); gii.oooszo@gmail.com (M.I.)
[2] Department of Chemistry, Osaka University, 1-13 Machikaneyama-cho, Toyonaka, Osaka 560-0043, Japan; ukai.kazuki.ud1@ms.naist.jp
[3] The Museum of Osaka University, Osaka University, 1-13 Machikaneyama-cho, Toyonaka, Osaka 560-0043, Japan
[4] Center for Analytical Instrumentation, Chiba University, 1-33 Yayoi-cho, Inage-ku, Chiba 263-8522, Japan; masu@faculty.chiba-u.jp
[5] Nippon Steel Co., 20-1 Shintomi, Futtsu, Chiba 293-8511, Japan; kajiro.6ey.hiroshi@jp.nipponsteel.com
* Correspondence: ueda@museum.osaka-u.ac.jp (T.U.); kanoh@faculty.chiba-u.jp (H.K.); Tel.: +81-6-6850-5778 (T.U.); +81-43-290-2784 (H.K.)

Abstract: [Cu(4,4'-bipyridine)$_2$(BF$_4$)$_2$] (ELM-11), an elastic layer-structured MOF (metal-organic framework), is expected to be a sophisticated CO$_2$ reservoir candidate because of its high capacity and recovery efficiency for CO$_2$ sorption. While ELM-11 shows a unique double-step gate sorption for CO$_2$ gas, the dynamics of the structural transition have not yet been clarified. In this study, the dynamics of the 4,4'-bipyridine linkers and the BF$_4^-$ anions were studied by determining ^{1}H spin-lattice relaxation times (T_1). The ELM-11 structural transition accompanying CO$_2$ sorption was also examined through the CO$_2$ uptake dependence of the ^{1}H spin–spin relaxation time (T_2), in addition to T_1. In its closed form, the temperature dependence of the ^{1}H T_1 of ELM-11 was analyzed by considering the contributions of both paramagnetic and dipolar relaxations, which revealed the isotropic reorientation of BF$_4^-$ and the torsional flipping of the 4,4'-bipyridine moieties. The resultant activation energy of 32 kJ mol^{-1} for the isotropic BF$_4^-$ reorientation is suggestive of strong (B-F...Cu^{2+}) interactions between Cu(II) and the F atoms in BF$_4^-$. Furthermore, the CO$_2$ uptake dependence of T_1 was found to be dominated by competition between the increase in the longitudinal relaxation time of the electron spins and the decrease in the spin density in the unit cell.

Keywords: metal-organic framework; elastic layer-structured MOF; gate sorption; ^{1}H NMR; spin–lattice relaxation time; spin–spin relaxation time; T_1; T_2; paramagnetic relaxation; dipolar relaxation

1. Introduction

Porous metal-organic frameworks (PMOFs) and porous coordination polymers (PCP), which exhibit dynamic structural transitions attributed to soft interactions in their crystal structures, are expected to have sorption properties that are different to those of traditional porous materials [1–3]. One of the most interesting phenomena in a flexible MOF is its guest-induced structural transition, which typically occurs at a threshold gas pressure and leads to an abrupt increase in the sorption isotherm, a phenomenon referred to as "breathing" and "gate sorption" [4–10]. The breathing of

MIL-53 involves micropore filling accompanied by structural shrinkage and swelling, with volume expansion [7,8]. The gate sorption of a layer-structured MOF is accompanied by an abrupt increase and decrease in the sorbed quantity at a definite pressure, with almost no sorption below the threshold pressure [4–6,11–15]. Such guest-induced framework transitions have also been studied using theoretical and computational methods [8,16–18]. With such novel properties, these materials are expected to be developed into a unique class of material for gas separation and molecular sensing technologies [4,19–23].

The gate sorption of $[Cu(4,4'\text{-bipyridine})_2(BF_4)_2]$ (ELM-11), an elastic layer-structured MOF, is a representative example of novel sorption behavior. This material shows unique sorption isotherms for CO_2, N_2, and CH_4 through the expansive modulation of its layer structure [4,24–29]. ELM-11 also exhibits a better capacity and recovery efficiency for CO_2 sorption compared to other nanoporous materials [9,26]. Layer stacking is stabilized by soft interactions, such as π–π interactions and H...F hydrogen bonds [11,24]. ELM-11 shows a double-step gate sorption for CO_2 gas [28]. The first gate-opening occurs at a relative pressure (P/P_0) of 0.003 at 195 K, accompanied with a 28% increase in the interlayer distance, while the second sorption occurs at $P/P_0 = 0.3$ with a 56% expansion from the initial interlayer distance. More detailed structural analyses provided its fine structures before and after CO_2 sorption [29].

The crystal structures of ELM-11 with different CO_2 uptake levels were studied by Hiraide et al in the 195–298 K temperature range using in situ synchrotron X-ray powder diffractometry. For example, the unit cell of **1**, the closed form of ELM-11 before CO_2 sorption, is monoclinic (space group $C2/c$, No. 15) with lattice constants: $a = 1.24227(8)$ nm, $b = 1.11618(6)$ nm, $c = 1.61420(11)$ nm, $\beta = 100.534(4)°$ at 273 K, and includes four formula units ($Z = 4$) [12]. By encapsulating two CO_2 molecules per $[Cu(bpy)_2(BF_4)_2]$ (bpy = 4,4'-bipyridine) monomer unit at 273 K, the closed form of ELM-11 transforms into ELM-11⊃$2CO_2$ (**2**), which corresponds to the first gate-opening process. In this transformation, the unit cell expands along its a- and c-axes: $a = 1.36851(6)$ nm, $b = 1.10446(3)$ nm, $c = 1.87175(6)$ nm, $\beta = 95.687(3)°$, although the crystal system and the space group are the same as those of the closed form. The CO_2 molecules penetrate through 1D channels composed of stacked square grids after expansion, and are then accommodated into the interlayer void spaces formed between the neighboring layered square grids through extension of the interlayer distance. The second gate-opening process accompanies the structural transition into ELM-11⊃$6CO_2$ (**3**), in which six CO_2 molecules are encapsulated in the $[Cu(bpy)_2(BF_4)_2]$ monomer unit at 195 K. In this form, the unit cell is triclinic (space group $P1$, No. 1), with lattice constants: $a = 1.10894(7)$ nm, $b = 1.11193(5)$ nm, $c = 1.43930(9)$ nm, $\alpha = 86.608(6)°$, $\beta = 75.513(5)°$, and $\gamma = 86.791(9)°$, and includes two formula units ($Z = 2$) [29]. The lattice volume with four included formula units expands from 2.2005(3) nm^3 for the closed form at 273 K to 3.4274(4) nm^3 for ELM-11⊃$6CO_2$ via 2.8157(2) nm^3 for ELM-11⊃$2CO_2$. Similar to the increase in the interlayer distance, the lattice volume is also 28% larger following the first step, and 56% larger following the second, compared with that of the closed form. Understanding the dynamic structure of its component moieties, such as the 4,4'-bipyridine linkers and BF_4^- anions, is necessary in order to clarify the transition mechanism of ELM-11 that accompanies gate sorption from a microscopic viewpoint. In addition, magnetic spin interactions between the paramagnetic spins will play important roles that induce the structural phase transition.

Electron-paramagnetic resonance (EPR) spectroscopy is a standard analytical procedure used to examine the local structures and spin–spin interactions in paramagnetic MOFs. The first EPR and [11]B magic-angle spinning (MAS) nuclear magnetic resonance (NMR) spectra were acquired by Jiang et al, and revealed the reversible structural changes that occur during the adsorption and desorption of probe molecules (CH_3OH and CH_3CN) [30]. Furthermore, Kultaeva et al. studied the formation and transformation mechanism of ELM-11 using powder and single-crystal EPR spectroscopy [31]. Based on the principal value of the g tensor and its anisotropy, they found that the cupric ions have elongated octahedral coordination symmetries and different axial ligands in the as-synthesized and activated forms of both $[Cu(bpy)_2(CH_3OH)_2](BF_4)_2$ and $[Cu(bpy)_2(CH_3CN)_2](BF_4)_2$.

Recently, the nuclear spin–lattice relaxation rates in paramagnetic substances have attracted much attention due to interest in distance-geometry [32], MRI-relaxation-agents [33], and quantum-computation [34] applications. The molecular motions, phase transitions, and inter-spin interactions in paramagnetic materials have been discussed through ^{1}H spin-lattice relaxation times (T_1) [35–38]. Therefore, ^{1}H nuclear magnetic relaxation in ELM-11 is expected to provide useful information about the structural changes and spin–spin interactions that accompany CO_2 gate sorption.

In this study, we investigated the dynamic behavior of the 4,4′-bipyridine linkers and the BF_4^- anions in the closed form of ELM-11 by determining its temperature-dependent ^{1}H spin-lattice relaxation times (T_1), after which the structural transition of ELM-11 accompanying CO_2 sorption was examined by the CO_2 uptake dependence of the ^{1}H spin–spin relaxation time (T_2) as well as T_1. Finally, the structural change due to CO_2 sorption was examined in terms of magnetic dipolar interactions between nuclear spins and between paramagnetic spins.

2. Experimental

ELM-11 was prepared according to the reported method [27]. After pretreatment under vacuum (<0.1 Pa) at 373 K for 10 h, CO_2 sorption isotherms were obtained volumetrically at 273 and 195 K using BELSORP Mini II (MicrotracBEL Corp., Osaka, Japan) instruments. The CO_2 gas was 99.9999% pure.

The NMR sample was prepared as follows: a 300 mg sample of ELM-11 powder was introduced into a glass NMR tube (ϕ 10 mm) and maintained under vacuum at 373 K for 10 h. CO_2 gas was loaded into the tube at 273 or 195 K and adjusted to the appropriate pressure. The tube was sealed with a valve and then inserted into the NMR spectrometer, with the temperature controlled at 273 or 195 K.

A JNM-MU25 pulse NMR spectrometer (JEOL, Akishima, Tokyo, Japan) with a ^{1}H resonance frequency of 25 MHz (0.5872 T, permanent magnet) was used to measure ^{1}H relaxation times. T_1 values were measured with the inversion recovery method using a radio-frequency pulse width of 2 μs, a repetition time of 2 ms, and 50 datapoints with a sampling interval of 30 μs. T_2 values were measured with the solid-echo method using a radio-frequency pulse width of 2 μs, a repetition time of 2 ms, and 500 datapoints with a sampling interval of 0.2 μs.

3. Results and Discussion

3.1. CO₂ Sorption Isotherms

CO_2 sorption isotherms for ELM-11 at 273 and 195 K are shown in Figure 1. The CO_2 sorption isotherm of ELM-11 to P/P_0 ~0.03 at 273 K reveals a vertical uptake at P/P_0 ~0.01 (Figure 1a), which corresponds to gate opening, as previously reported [4,24,26,27]. Another steep increase in sorption is seen at 195 K at P/P_0 ~0.3, as shown in Figure 1b. Similar double-step sorption isotherms have previously been reported [13,14,28,29]. Detailed structural analyses showed that ELM-11 absorbs two CO_2 molecules per Cu atom to form **2**, with a 28% expansion in the interlayer distance at the first step at 273 K, and absorbs four more CO_2 molecules per Cu atom to form **3**, with a 56% expanded layer structure compared to the initial structure at 195 K [28,29].
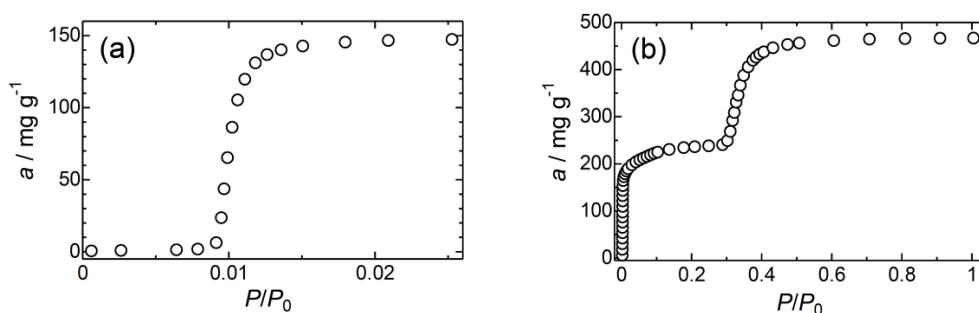

Figure 1. CO_2 sorption isotherms for ELM-11 at (**a**) 273 K and (**b**) 195 K.

3.2. Calculating the Second Moment Plateau Values

The van Vleck formula can be used to calculate NMR second moments in rigid lattices of solid-state materials with well-known molecular and crystal structures [39,40]. A theoretical description of the NMR second moment is given in Appendix A. Using the above-mentioned formula, we calculated the ^{1}H and ^{19}F second moments of the rigid lattices of the three crystal structures of ELM-11. Second-moment reductions were also calculated by taking into account the anisotropy parameter [40,41] associated with the isotropic reorientation of BF_4^- and the torsional flipping of the 4,4′-bipyridine linkers. The second moments in the rigid lattices determined for the ^{1}H and ^{19}F nuclei are summarized in Tables A1 and A2 in Appendix A, while Tables 1 and 2 show the evaluated reductions in the ^{1}H and ^{19}F second moments.

Table 1. Reductions in the ^{1}H second moments (in 10^{-8} T^2) in ELM-11.

Interaction	Motional Mode		
	bpy Flip	BF_4^- Rotation	bpy Flip + BF_4^- Rotation
1			
bpy 1			
$\Delta M_{2,intra}^{HH}$	0	0	0
$\Delta M_{2,inter}^{HH}$	1.538	0	1.538
$\Delta M_{2,inter}^{HF}$	0	0.525	0.525
total	1.538	0.525	2.063
bpy 2			
$\Delta M_{2,intra}^{HH}$	0.452	0	0.452
$\Delta M_{2,inter}^{HH}$	0.565	0	0.565
$\Delta M_{2,inter}^{HF}$	0.44	0.384	0.566
total	1.457	0.384	1.583
2			
bpy 1			
$\Delta M_{2,intra}^{HH}$	0	0	0
$\Delta M_{2,inter}^{HH}$	0.015	0	0.015
$\Delta M_{2,inter}^{HF}$	0	0.664	0.664
total	0.015	0.664	0.679
bpy 2			
$\Delta M_{2,intra}^{HH}$	0.223	0	0.223
$\Delta M_{2,inter}^{HH}$	0.126	0	0.126
$\Delta M_{2,inter}^{HF}$	0.373	0.232	0.558
total	0.722	0.232	0.907
3			
bpy 1			
$\Delta M_{2,intra}^{HH}$	0	0	0
$\Delta M_{2,inter}^{HH}$	0.092	0	0.092
$\Delta M_{2,inter}^{HF}$	0	0.342	0.342
total	0.092	0.342	0.434
bpy 2			
$\Delta M_{2,intra}^{HH}$	1.157	0	1.157
$\Delta M_{2,inter}^{HH}$	0.02	0	0.02
$\Delta M_{2,inter}^{HF}$	0	0.244	0.244
total	1.177	0.244	1.421

Table 1. *Cont.*

Interaction	Motional Mode		
	bpy Flip	BF$_4^-$ Rotation	bpy Flip + BF$_4^-$ Rotation
bpy 1'			
$\Delta M_{2,intra}^{HH}$	1.337	0	1.337
$\Delta M_{2,inter}^{HH}$	0.185	0	0.185
$\Delta M_{2,inter}^{HF}$	0	0.309	0.309
total	1.522	0.309	1.831
bpy 2'			
$\Delta M_{2,intra}^{HH}$	0.587	0	0.587
$\Delta M_{2,inter}^{HH}$	0.267	0	0.267
$\Delta M_{2,inter}^{HF}$	0.361	0.208	0.428
total	1.215	0.208	1.282
bpy 1			
$\Delta M_{2,intra}^{HH}$	0	0	0
$\Delta M_{2,inter}^{HH}$	0.092	0	0.092
$\Delta M_{2,inter}^{HF}$	0	0.342	0.342
total	0.092	0.342	0.434

Table 2. Reductions in the ^{19}F second moments (in 10^{-8} T^2) in ELM-11.

Interaction	Motional Mode		
	bpy Flip	BF$_4^-$ Rotation	bpy Flip + BF$_4^-$ Rotation
1			
$\Delta M_{2,intra}^{FF}$	0	6.507	6.507
$\Delta M_{2,inter}^{FF}$	0	4.503	4.503
$\Delta M_{2,inter}^{FH}$	1.117	2.309	2.774
$\Delta M_{2,intra}^{F10B}$	0	0.757	0.757
$\Delta M_{2,intra}^{F11B}$	0	8.66	8.660
total	1.117	22.736	23.201
2			
$\Delta M_{2,intra}^{FF}$	0	6.337	6.337
$\Delta M_{2,inter}^{FF}$	0	6.396	6.396
$\Delta M_{2,inter}^{FH}$	0.270	2.278	2.736
$\Delta M_{2,intra}^{F10B}$	0	0.729	0.729
$\Delta M_{2,intra}^{F11B}$	0	8.343	8.343
total	0.270	24.083	24.541
3			
$\Delta M_{2,intra}^{FF}$	0	5.478	5.478
$\Delta M_{2,inter}^{FF}$	0	2.771	2.771
$\Delta M_{2,inter}^{FH}$	3.816	2.765	4.994
$\Delta M_{2,intra}^{F10B}$	0	0.628	0.628
$\Delta M_{2,intra}^{F11B}$	0	7.189	7.189
total	3.816	18.831	21.06

The reduction in the ^{1}H second moment, ΔM_2^H, which is the sum of $\Delta M_{2,\ intra}^{HH}$, $\Delta M_{2,\ inter}^{HH}$ and $\Delta M_{2,\ inter}^{HF}$, is about $(0.4–2) \times 10^{-8}$ T^2, which indicates a low contribution to the total magnetic

dipolar relaxation rate. On the other hand, the reduction in the ^{19}F second moment, ΔM_2^F, which is the sum of $\Delta M_{2,\ intra}^{FF}$, $\Delta M_{2,\ inter}^{FF}$, $\Delta M_{2,\ inter}^{FH}$, and $\Delta M_{2,\ intra}^{FB}$, ranged between 21×10^{-8} and 24×10^{-8} T^2. In particular, the isotropic reorientation of BF$_4^-$ effectively modulates the F-F and F-B vectors, leading to a large reduction in the second moment, which suggests that spin–lattice relaxation is expected to be effective through a mechanism involving fluctuations in magnetic dipolar interactions that act on ^{19}F nuclei and control the ^{1}H spin–lattice relaxation rate through cross-relaxation between the ^{1}H and ^{19}F spin systems.

3.3. Temperature Dependence of T_1 in the Closed form of ELM-11

Figure 2a shows the temperature dependence of ^{1}H T_1 in **1**. Below 250 K, T_1 was almost constant, at 520 μs; it decreased above 250 K and then increased to 499 μs at 360 K after exhibiting a minimum value of 492 μs at 323 K. T_1 only changed by 30 μs in this region, which is only a 5.8% change compared to the original value of 520 μs. If the T_1 minimum is caused by the thermal motions of BF$_4^-$ and/or 4,4′-bipyridine, then the apparent activation energy (0.5 kJ mol^{-1}) is much smaller than the reported E_a values for the isotropic rotation of BF$_4^-$ (10–26 kJ mol^{-1}) [40,42–44] and/or the torsional flipping of 4,4′-bipyridine (~10 kJ mol^{-1}) [45,46].

ELM-11 contains paramagnetic Cu^{2+} ($S = 1/2$) ions and four kinds of NMR-active nucleus: ^{1}H ($I = 1/2$), ^{19}F ($S = 1/2$), ^{10}B ($S = 3$), and ^{11}B ($S = 3/2$). In this case, the nuclear spin systems relax through two mechanisms: paramagnetic and dipolar relaxation. In general, relaxation times through paramagnetic ions are one or two orders of magnitude shorter than the relaxation times of diamagnetic substances. According to the multi-paramagnetic-center model, which is preferred for paramagnetic materials with dense paramagnetic-centers, the paramagnetic relaxation rate (R_{1p}) is given by [47,48].

$$R_{1p} = 2\overline{C}N_p^2 + 50\left(\overline{C}D\right)^{1/2}N_p^{4/3}, \tag{1}$$

where $\overline{C}$ and D is the efficiency of direct relaxation and the diffusion coefficient for spin diffusion, respectively, and N_p is the number of paramagnetic centers per unit volume of the sample. In the powder sample, $\overline{C}$ is represented by

$$\overline{C} = \frac{2}{5}\left(\frac{\mu_0}{4\pi}\right)^2 S(S+1)\gamma_S^2\gamma_I^2\hbar^2 \frac{\tau_e}{1+\omega_I^2\tau_e^2}, \tag{2}$$

where γ_S and γ_I are the gyromagnetic ratios of the electron spin and resonant nuclei, respectively, S is the spin of the paramagnetic ion, τ_e is the correlation time for the z-component of the paramagnetic spin (longitudinal relaxation time for the electron spin), and ω_I is the resonance frequency of a resonant nucleus. According to Bloembergen [49], $D = a^2/50T^2$, where a is the average ^{1}H-^{1}H distance (0.551 nm for **1**) and T_2 is the ^{1}H spin–spin relaxation time (average of experimental values; ~22 μs). As a result, $D = 2.87 \times 10^{-16}$ m^2 s^{-1} for **1**. This is reasonable because it is of the same order of magnitude as the D value (6.25×10^{-16} m^2 s^{-1}) for the high spin state of [Fe(ptz)$_6$](BF$_4$)$_2$ (ptz = 1-*n*-propyl-1*H*-tetrazole) [35]. Furthermore, we evaluated N_p as 1.91×10^{27} m^{-3} for the body-centered lattice formed by the Cu^{2+} ions in **1**. Thus, R_{1p} depends strongly on τ_e.

On the other hand, the dipolar relaxation rate (R_{1d}) is mainly controlled by fluctuations in the magnetic dipolar interactions among the ^{1}H ($I = 1/2$), ^{19}F ($S = 1/2$), ^{10}B ($S = 3$), and ^{11}B ($S = 3/2$) spins. In such a multi-spin system, cross relaxation between the ^{1}H, ^{19}F, ^{10}B, and ^{11}B nuclei are taken into account [40]. Here, assuming that both the ^{1}H and ^{19}F nuclei dominantly contribute to cross relaxation because of their large gyromagnetic ratios, the actual relaxation rates are given by the eigenvalues of the relaxation matrix **R** [43,44,50–52]:

$$\boldsymbol{R} = \begin{bmatrix} R_{HH} & R_{HF} \\ R_{FH} & R_{FF} \end{bmatrix}. \tag{3}$$

In general, these relaxation rates lead to the non-exponential recovery of magnetization: however, the ^{1}H magnetization recovers exponentially in ELM-11. In this context, as mentioned in Appendix B, we can regard R_{HH}, $R_{FF} \approx R_{FH}$, R_{HF}; hence one of the two eigenvalues is almost zero. The observed relaxation rate then takes the following form

$$(R_{1d})_{HH} = (R_{1d})_{FF} = R_{HH} + R_{FF}, \tag{4}$$

where R_{HH} and R_{FF} are diagonal elements of the relaxation matrix **R**. In this case, R_{HH} and R_{FF} are given by [39,40]:

$$R_{HH} = \frac{2}{3}\gamma_H^2 \Delta M_2^{HH} g_1(\omega_H, \tau_H) + \frac{1}{2}\gamma_H^2 \Delta M_2^{HF} g_2(\omega_H, \omega_F, \tau_H), \tag{5a}$$

$$R_{FF} = \quad \frac{2}{3}\gamma_H^2 \Delta M_2^{FF} g_1(\omega_F, \tau_F) + \frac{1}{2}\gamma_F^2 \Delta M_2^{FH} g_2(\omega_F, \omega_H, \tau_F) + \frac{1}{2}\gamma_F^2 \Delta M_2^{F10B} g_2(\omega_F, \omega_{10B}, \tau_F)$$
$$+ \frac{1}{2}\gamma_F^2 \Delta M_2^{F11B} g_2(\omega_F, \omega_{11B}, \tau_F) \tag{5b}$$

The analytical formulas for $g_1(\omega_i, \tau_i)$ and $g_2(\omega_i, \omega_j, \tau_i)$ are given by [40,50]:

$$g_1(\omega_i, \tau_i) = \frac{\tau_i}{1 + \omega_i^2 \tau_i^2} + \frac{4\tau_i}{1 + 4\omega_i^2 \tau_i^2}, \tag{6a}$$

$$g_2(\omega_i, \omega_j, \tau_i) = \frac{\tau_i}{1 + (\omega_i - \omega_j)^2 \tau_i^2} + \frac{3\tau_i}{1 + \omega_i^2 \tau_i^2} + \frac{6\tau_i}{1 + (\omega_i + \omega_j)^2 \tau_i^2}. \tag{6b}$$

Assuming that a thermal activation process is responsible for the fluctuation in the internuclear vector, the temperature dependence of τ_i (i = H, F) is given by the Arrhenius equation, as follows

$$\tau_i = \tau_{0,i} \exp(E_{a,i}/RT), \tag{7}$$

where $E_{a,i}$ (i = H, F) is the activation energy for BF_4^- and 4,4′-bipyridine. Consequently, we analyzed the temperature dependence of ^{1}H T_1 using the sum of the contributions from both paramagnetic relaxation (R_{1p}) and dipolar relaxation (R_{1d}):

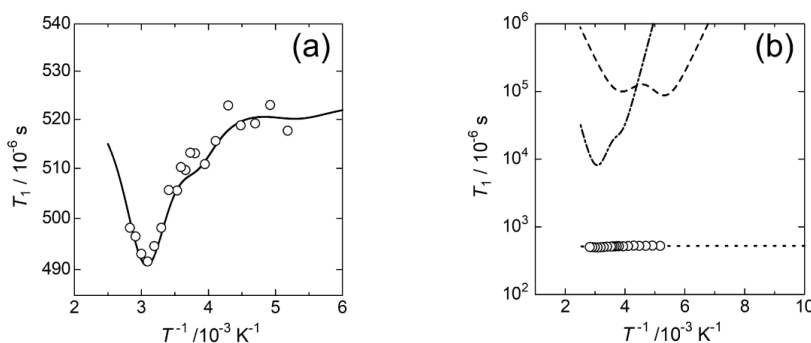$$R_{1H} = 1/T_{1H} = R_{1p} + R_{1d}. \tag{8}$$

The experimental data were fitted to Equation (8), the results of which are shown in Figure 2a,b. The R_{1p} component was optimized at $\tau_e = 1.22 \times 10^{-11}$ s, resulting in a T_{1p} value more than one order of magnitude smaller than T_{1d}. The evaluated τ_e value is reasonable because typical τ_e values for paramagnetic metal ions range between 10^{-8} s and 10^{-12} s [53]; it is also sufficiently fast to average out the width of the ^{1}H resonance line due to ^{1}H-electron dipolar interactions. As described below, the average value of ^{1}H T_2 is about 22 μs, which corresponds to a full width at half maximum (FWHM) of 15 kHz, where FWHM = $1/\pi T_2$. This value is much narrower than the linewidth (~500 kHz) caused by the average local magnetic field between interlayer Cu-H pairs. Table 3 summarizes the activation parameters and ΔM_2^{ii} and ΔM_2^{ij} values for the isotropic rotation of BF_4^- and the torsional flipping of 4,4′-bipyridine. The ΔM_2^{ii} and ΔM_2^{ij} values determined from the optimization of R_{1d} are in good agreement with those calculated assuming an isotropic BF_4^- reorientation and the torsional flipping of 4,4′-bipyridine. This observation suggests that the T_1 minimum observed at 323 K is mainly caused by averaging the ^{19}F-^{19}F and ^{19}F-^{11}B magnetic dipolar interaction by isotropic BF_4^- reorientation. On the other hand, the small dips observed at 200 and 250 K are attributed to the averaging of the ^{1}H-^{1}H and ^{1}H-^{19}F magnetic dipolar interactions by the torsional flipping of the 4,4′-bipyridine as well as isotropic BF_4^- reorientation. That is, the ^{1}H-^{1}H and ^{1}H-^{19}F magnetic dipolar interactions contribute less to the total T_1 compared to the ^{19}F-^{19}F and ^{19}F-^{11}B magnetic dipolar interactions; hence, the calculated T_1 curve is less sensitive to the 4,4′-bipyridine activation

parameters. Therefore, in order to improve the reliability of the optimization results and to guarantee that the parameters have physical meaning, we assumed an E_a value for the torsional flipping of the 4,4′-bipyridine. In fact, Moreau et al. reported that the torsional barrier for phenylene rings within linkers in a series of isoreticular octacarboxylate MOFs depended on the steric hindrance around the linkers, as well as the electronic structure of the framework [54]. Furthermore, Inukai et al. reported that in [{Zn(5-nitroisophthalate)$_x$ (5-methoxyisophthalate)$_{1-x}$ (deuterated 4,4′-bipyridyl)} (DMF·MeOH)]$_n$, a kind of flexible PCP referred to as "CID-5/6", the energy barrier for the rotation of the pyridyl ring depended on the steric hindrance around the linkers: the E_a values for the 4-site and 2-site flip rotations are 20 and 25 kJ mol^{-1} for CID-5/6 (x = 0.55), and 32 and 27 kJ mol^{-1} for CID-5/6 (x = 0.37) [55]. In the latter case, the intermolecular distances between 4,4′-bipyridine linkers in CID-5 and 6 are 4.11 Å and 3.91 Å, whereas it is 6.21 Å in the closed form of ELM-11, which suggests that there is less steric hindrance between the linkers in ELM-11. Therefore, we referred to the E_a value as reported in the gas phase (4.0 kcal mol^{-1}) [45] for simplicity, and then fixed the E_a value to be close to this value during our T_1 analysis.

As a result, the E_a value (32 kJ mol^{-1}) obtained for the isotropic reorientation of BF$_4$$^-$ is slightly larger than those (10–26 kJ mol^{-1}) reported in various systems [40,42–44]. The relatively short Cu-F interatomic distance of 2.404 Å facilitates the formation of a strong hydrogen-bond-like interaction (C-F...M$^+$ [56]) between Cu(II) and a F atom in BF$_4$$^-$ (B-F...Cu^{2+}). As a result, the BF$_4$$^-$ isotropic reorientation in ELM-11 has a large E_a value.

The gate phenomenon is closely associated with lattice vibration as well as the diffusivity of gas molecules. The rotational flipping of the 4,4′-bipyridine moiety is a type of phonon acoustic lattice-vibration mode of ELM-11. Gas molecules, such as CO$_2$, perturb the rotational motion of the 4,4′-bipyridine moiety through molecular collisions. In particular, the inelastic collisions between gas molecules and the ELM-11 framework is considered to effectively perturb the thermally activated rotational motion of the 4,4′-bipyridine moiety, which then triggers the structural transition for gate opening. Thus, energy-transfer efficiency between the gas molecules and the ELM-11 framework determines the gate-opening pressure.

Furthermore, the torsional flipping and/or rotational motion of the 4,4′-bipyridine moiety also affects the orientational selectivity of the CO$_2$ molecules toward molecular diffusion and arrangement in **1** at the first gate opening. Torsional flipping gives rise to an excluded volume for the pyridyl ring that is larger than the rigid one. This reduces the effective free volume along the *b*-axis because twisted 4,4′-bipyridine moieties lie along the *b*-axis. As a result, the accessible space for the CO$_2$ molecules elongates along the *b*-axis as a prolate spheroid, which not only affects the molecular orientation when CO$_2$ molecules penetrate into the ELM-11 crystal lattice, but also facilitates the alignment of CO$_2$ molecules along the *b*-axis. In fact, the CO$_2$ molecules are accommodated in the interlayer void spaces formed between the neighboring layered square grids in **2**, which results in the alignment of the molecular axes with the *b*-axis.

Figure 2. ^{1}H spin-lattice relaxation time (T_1) for the closed form of ELM-11 as a function of reciprocal temperature: (**a**) expanded and (**b**) overall views. The solid line in (**a**) is the result of fitting to Equation (8). The dotted, dashed, and chain-dotted lines are R_{1p}, R_{HH}, and R_{FF}, respectively.
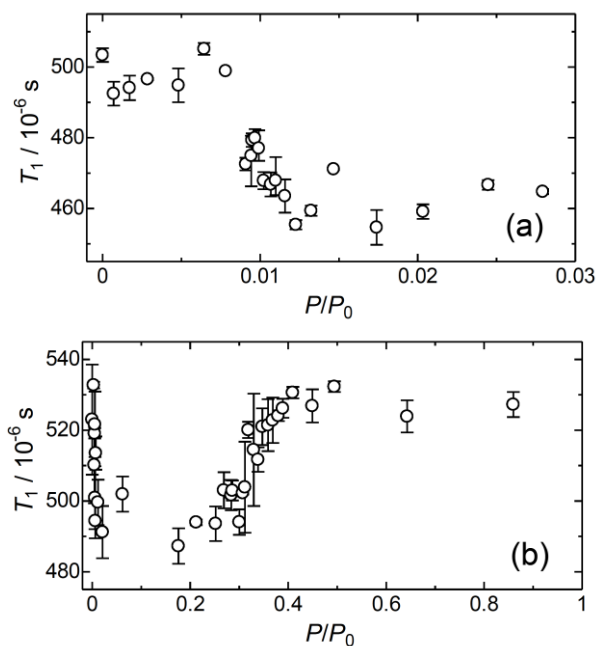
Table 3. Activation parameters for the isotropic reorientation of BF_4^- and the torsional flipping of 4,4′-bipyridine in **1** determined from dipolar relaxation data.

Parameter	Expt.	Calc.
^{1}H interaction		
$\tau_{H,0}/s$	1.0×10^{-12}	——
$E_a(H)/kJ\ mol^{-1}$	18	——
$\Delta M_2^{HH}/10^{-8}\ T^2$	1.28	1.28
$\Delta M_2^{HF}/10^{-8}\ T^2$	0.55	0.55
^{19}F interaction		
$\tau_{F,0}/s$	4.0×10^{-14}	——
$E_a(F)/kJ\ mol^{-1}$	32	——
$\Delta M_2^{FF}/10^{-8}\ T^2$	10	11.0
$\Delta M_2^{FH}/10^{-8}\ T^2$	1.6	2.77
$\Delta M_2^{F11B}/10^{-8}\ T^2$	7.0	8.66
$\Delta M_2^{F10B}/10^{-8}\ T^2$	0.61	0.76

3.4. CO_2-Uptake Dependence of T_1 in ELM-11

Figure 3a,b shows the dependence of ^{1}H T_1 on the amount of CO_2 sorbed into ELM-11 at 273 and 195 K, respectively. The T_1 value was observed to decrease in a stepwise manner at 273 K, from 500 to 455 μs at $P/P_0 = 0.01$. On the other hand, the T_1 value decreased in a stepwise manner at 195 K, from 532 to 490 μs at $P/P_0 = 0.01$, and then increased again to 529 μs in the 0.2–0.4 P/P_0 range. These observed changes are in good agreement with the stepwise increases in the uptake of CO_2 shown in the sorption isotherms (Figure 1). The crystal structure of ELM-11 changes through the stepwise sorption of CO_2, resulting in an increase in the interlayer distance. Therefore, this feature suggests that variations in T_1 due to CO_2 sorption are closely related to the structural changes undergone by ELM-11. Table 4 lists the T_1 values for each ELM-11 structure at 273 and 195 K. The T_1 changes observed between 529 and 455 μs are due to structural changes, and the change in T_1 during a one-step structural change is in the 39–45 μs range.

Figure 3. ^{1}H T_1 as a function of the relative pressure of CO_2 under sorption equilibrium with ELM-11 at: (**a**) 273 K and (**b**) 195 K.

T_1 appears to depend on CO_2 uptake, which is ascribable to: (1) an increase in the interlayer distance, and (2) an increase in the chemical pressure due to the impact of CO_2 on the molecular motions of BF_4^- and 4,4′-bipyridine. The change in T_1 in **1** in moving from 250 to 323 K is about 32 μs, which is smaller than those observed for the CO_2-uptake dependence. Since ΔM_2^{F11B} dominates ΔM_2, a further increase in ΔM_2^{F11B} is required in order to explain the relationship between T_1 and CO_2 uptake. However, the structure of BF_4^- is not significantly affected by changes in the crystal structure of ELM-11; consequently, isotropic BF_4^- reorientation cannot be used to reasonably explain the observed change in T_1 due to CO_2 sorption.

On the other hand, the increase in the interlayer distance between the stacked two-dimensional $[Cu(bpy)_2^{2+}]_n$ sheets increases the unit cell volume and the interlayer Cu-Cu distance; these affect N_p and τ_e, which dominate R_{1p}. Since R_{1p} depends on N_p^2 and $N_p^{4/3}$ [47], an increase in the cell volume decreases N_p (see Table 4), resulting in a decrease in R_{1p}. In contrast, τ_e is affected by interactions between electron spins (dipolar interactions and/or exchange interactions) and, as a first approximation, $1/\tau_e$ is proportional to the magnetic dipolar and/or exchange interaction [53]. The average Cu-Cu distance in a $[Cu(bpy)_2^{2+}]_n$ layer is 1.11 nm, whereas the average Cu-Cu distance between layers is 0.9105 nm in **1**, 0.9959 nm in **2**, and 1.0692 nm in **3**. This feature strongly suggests that interlayer spin–spin interactions dominate more than intralayer ones. Since the magnetic dipolar and exchange interactions decay with increasing inter-spin distance, τ_e increases with inter-spin distance. Consequently, the change in T_1 due to CO_2 sorption can be examined using τ_e as a variable.

Table 4 summarizes the experimental and calculated values of T_1 for each crystal structure. $T_{1p, calc}$ was calculated using τ_e as a variable so as to reproduce $T_{1p, exp}$. At 273 K, the experimental value for **1** is somewhat smaller than the calculated one; this difference stems from the contribution of R_{1d}. Compared to τ_e at 195 K, a longer interlayer Cu-Cu distance leads to a longer τ_e. Thus, expansion of the unit cell due to CO_2 sorption decreases the spin density, whereas elongation of the interlayer distance increases τ_e. These two effects act on T_{1p} in opposite directions, and in ELM-11 they are balanced and determine the total T_{1p} of the system. The T_{1p} of **2** is shorter than that of **1** because the contribution of τ_e is rather large. On the other hand, both effects are comparable in **3** and, as a result, its T_{1p} is almost the same as that of **1**.

Table 4. ^{1}H T_1 via paramagnetic centers, electron longitudinal relaxation times, diffusion coefficients for spin diffusion, spin densities, and average interlayer Cu-Cu distances in ELM-11.

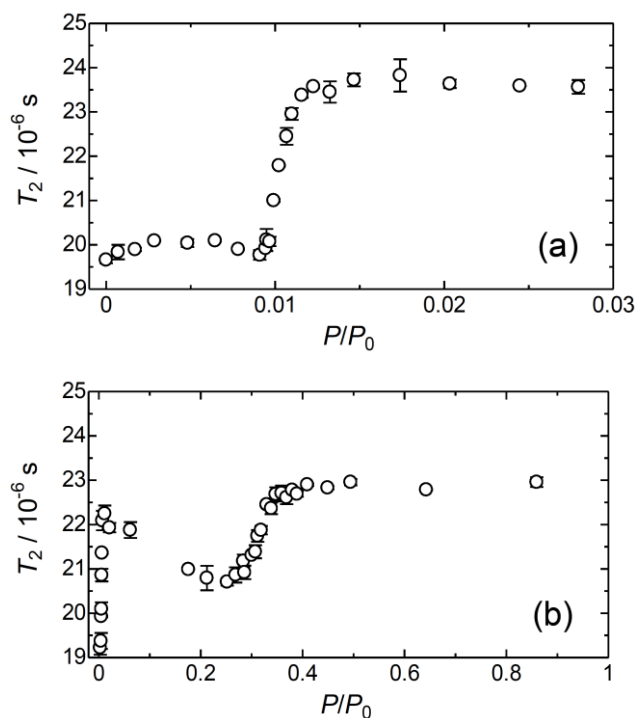| Parameter	1		2		3
T/K	273	195	273	195	195
$T_{1p, exp}$/μs	500	532	455	490	529
$T_{1p, calc}$/μs	523		449	490	528
τ_e/s	1.22×10^{-11}		3.08×10^{-11}	2.59×10^{-11}	4.05×10^{-11}
D/m^{2}s^{-1}	2.87×10^{-16}		2.87×10^{-16}		2.87×10^{-16}
N_p/m^{-3}	1.91×10^{27}		1.51×10^{27}		1.21×10^{27}
$r_{ave.}$(Cu-Cu)/nm	0.9105		0.9959		1.0692

3.5. Spin–Spin Relaxation Time (T_2) in ELM-11

Figure 4a,b shows the dependence of T_2 on the amount of CO_2 sorbed at 273 K and 195 K. At 273 K, ELM-11 shows a stepwise increase in T_2 at P/P_0 ~0.01, despite a decrease in T_1. On the other hand, ELM-11 shows two stepwise increases in T_2 at 195 K, at P/P_0 ~0.01 and ~0.3. These changes in T_2 also correspond to the gate sorption of CO_2, as was observed for T_1, which accompanies a structural change in the crystal structure, in particular, an increase in the interlayer distance. The spin system satisfies a condition that $\omega_H \tau \gg 1$ in these temperature regions, because $T_1 \neq T_2$ and $T_2 \ll T_1$; hence T_2 is governed by the local magnetic field at the ^{1}H nuclei ($1/T_2 \propto \langle B_{loc}^2 \rangle$). The local magnetic field caused by a spin with magnetic moment μ at a position far from the spin, is given by $(\mu_0/4\pi)(\mu/r^3)(3\cos^2\theta - 1)$ [39]. Here, θ is the angle between the inter-spin vector and the external magnetic field and μ_0 is the magnetic

permeability of a vacuum. The ^{1}H, ^{19}F, and electron spins contribute to the local magnetic field in ELM-11.

The magnitude of the local magnetic field is inversely proportional to the cube of the inter-spin distance. The contribution of Cu^{2+} can be evaluated from the average Cu-H distance between the stacked two-dimensional $[Cu(bpy)_2{}^{2+}]_n$ sheets, which is 0.7801 nm in **1**, 0.8668 nm in **2**, and 0.9702 nm in **3**. The square of the local magnetic field, B^2_{loc}, is evaluated using these distances to be 383×10^{-8} T^2, 203×10^{-8} T^2, and 103×10^{-8} T^2, respectively. Consequently, extending the interlayer distance results in a decrease in B^2_{loc} to 53% in **2**, and 27% in **3**, of that of **1**. Actually, the magnetic moment of Cu^{2+} is partially averaged out by the fast flip-flopping of the electron spin; hence, the net magnetic moment of Cu^{2+} reduces B^2_{loc} to $\langle B^2_{loc} \rangle$.

The contributions from the ^{1}H and ^{19}F magnetic moments can also be evaluated through the second moments in the rigid lattices (see Tables A1 and A2). **1** and **2** contain two kinds of 4,4′-bipyridine linkers with different conformations, whereas **3** has four kinds of 4,4′-bipyridine linker. The $M^{HH}_{2,intra}$ values for the two conformers of **1** are 7.348×10^{-8} T^2 and 2.086×10^{-8} T^2, while in **2** they are 5.683×10^{-8} T^2 and 1.958×10^{-8} T^2, and they are 8.454×10^{-8} T^2, 6.202×10^{-8} T^2, 6.093×10^{-8} T^2, and 2.357×10^{-8} T^2, for the four conformers of **3**. In each case, the conformer with the somewhat smaller torsion angle, in which ^{1}H-^{1}H distances are relatively short, gives a larger $M^{HH}_{2,intra}$ value than that with the larger torsion angle. Furthermore, the values of $M^{HH}_{2,inter}$ of the planar and twisted conformers are similar in each compound, but $M^{HH}_{2,inter}$ decreases in the order: **1** > **2** > **3**, which indicates that the intermolecular ^{1}H-^{1}H dipolar interaction is affected little by the conformation of the 4,4′-bipyridine moiety, but decreases due to the increase in the interlayer distance. On the other hand, $M^{FF}_{2,intra}$, $M^{FF}_{2,inter}$, $M^{FH}_{2,inter}$, $M^{F10B}_{2,intra}$, and $M^{F11B}_{2,intra}$ are almost identical in the rigid lattices of the three substances, which suggests that the increase in the interlayer distance affects the intermolecular ^{1}H-^{19}F dipolar interactions little. Therefore, ^{1}H-^{1}H dipolar interactions are also considered to be among the factors that affect T_2 through the local magnetic field.

Figure 4. ^{1}H T_2 as a function of the relative pressure of CO_2 under sorption equilibrium with ELM-11 at: (**a**) 273 K and (**b**) 195 K.

In terms of the structural changes that occur in going from **1** to **2** and then from **2** to **3**, increases in the interlayer distance and the conformational changes undergone by the 4,4′-bipyridine linkers decrease both the ^{1}H-electron and ^{1}H-^{1}H dipolar interactions, i.e., the local magnetic field around the protons, resulting in an increase in T_2. In addition, at 195 K, T_2 is somewhat lower for CO_2 sorption between the first and the second steps. Since no lattice shrinkage was observed by powder XRD to accompany the decrease in interlayer distance during this process, we infer that the decrease in T_2 is not related to a change in interlayer distance (i.e., the ^{1}H-electron distance). In fact, the closest ^{1}H-^{1}H distance in 4,4′-bipyridine, pairs of which contribute the most to the local magnetic field, changes periodically with torsion angle. The local field is smallest at a twist angle of 90°, in which two pyridine rings are perpendicular to each other, and is largest for the planar structure, with a twist angle of 0° or 180°. Hence, we speculate that the conformational change undergone by the 4,4′-bipyridine linkers is one of the origins of the observed decrease in T_2 between the first and the second CO_2-sorption steps. The CO_2 uptake during the first gate sorption is estimated to be 160 mg g^{-1}, which corresponds to the sorption of two CO_2 molecules per [Cu(bpy)$_2$](BF$_4$)$_2$ formula unit, after which the CO_2 uptake increases gradually with P/P_0, to a value of 230 mg g^{-1} just prior to the second gate sorption. This uptake corresponds to the sorption of 2.9 CO_2 molecules per ELM-11 formula unit. Furthermore, uptake was observed to increase to 500 mg g^{-1} following the second gate sorption, which corresponds to the sorption of 6.2 CO_2 molecules per ELM-11 formula unit. Hiraide et al. reported the crystal structures of **2** and **3**, and revealed that the torsion angle around the C-C axis becomes small as the structure transforms from **2** into **3** [11,29]. This feature is considered to avoid repulsion between CO_2 and 4,4′-bipyridine, which increases the amount of sorbed CO_2 because the planar 4,4′-bipyridine structure has less free volume around its linkers than the other conformers. In fact, the conformation of the 4,4′-bipyridine linkers reportedly approaches that of the planar conformer by reducing the torsional angles from 0.74° and 70.64° in **2** to 0.14° and 68.74° in ELM-11⊃3CO$_2$ [11,29]. As the molecular structure of 4,4′-bipyridine approaches planarity, the intramolecular ^{1}H-^{1}H distances (particularly, at the 2,6 and 2′,6′ positions) become shorter, which increases the ^{1}H-^{1}H magnetic dipolar interactions. This conclusion is also supported by the $M_{2,intra}^{HH}$ values of the 4,4′-bipyridine moieties, which are significantly different for the planar (5.683 × 10^{-8} T^2) and twisted (1.958 × 10^{-8} T^2) orientations. These $M_{2,intra}^{HH}$ values correspond to T_2 contributions of 13 and 22 μs. Therefore, the increase in the intramolecular ^{1}H-^{1}H dipolar interaction is regarded as a possible explanation for the decrease in T_2 observed between the first and second sorption steps.

4. Conclusions

We calculated the ^{1}H and ^{19}F second moments in the rigid lattices of the three crystal structures of ELM-11, and the reductions in the second moments due to both isotropic BF$_4^-$ reorientation and the torsional flipping of the 4,4′-bipyridine linkers. ^{1}H second-moment reductions of (0.4–2) × 10^{-8} T^2 were determined, indicative of a low contribution to the total magnetic dipolar relaxation rate. On the other hand, reductions of (21–24) × 10^{-8} T^2 were determined for the ^{19}F second moment. These large reductions suggested that ^{1}H spin–lattice relaxation effectively takes place through fluctuations in the magnetic dipolar interactions that act on ^{19}F nuclei through cross-relaxation between the ^{1}H and ^{19}F spin systems.

The temperature dependence of ^{1}H T_1 in the closed form of ELM-11 was analyzed using the sum of the contributions from both paramagnetic relaxation (R_{1p}) and dipolar relaxation (R_{1d}). We found that R_{1p} makes a dominant contribution to the total ^{1}H spin–lattice relaxation rate, but the T_1 minimum observed at 323 K is mainly due to the averaging of ^{19}F-^{19}F and ^{19}F-^{11}B magnetic dipolar interactions through isotropic BF$_4^-$ reorientation. The large E_a value (32 kJ mol^{-1}) obtained for the isotropic BF$_4^-$ reorientation supports the formation of a strong hydrogen-bond-like interaction (B-F...Cu^{2+}) between Cu(II) and a F atom in BF$_4^-$. We also discussed the role that torsional flipping of the 4,4′-bipyridine moiety plays in relation to the gate-opening phenomenon, as well as the orientational selectivity of the CO_2 molecules in relation to their diffusion and arrangement in the lattice.

The dependence of T_1 on CO_2 uptake is the result of a corresponding increase in the interlayer distance. The increase in the unit cell volume due to CO_2 sorption led to a decrease in spin density, whereas an increase in the interlayer distance resulted in an increase in the longitudinal relaxation time of the electron spins (τ_e). These two effects, which act on T_{1p} in opposite directions, balance each other and control the T_1 value.

The local magnetic field at the ^{1}H nuclei governs the T_2 value, and a decrease in the local magnetic field increases the T_2 value. The local magnetic field associated with the net magnetic moments of Cu^{2+} and the intermolecular ^{1}H dipolar interaction decreases with increasing interlayer distance in ELM-11, leading to an increase in T_2. Furthermore, the conformational change in the 4,4'-bipyridine unit, from the twisted form to the planar form, enables the intramolecular ^{1}H dipolar interaction to increase, which shortens T_2.

Appendix A. Calculating Second Moments for ELM-11

Appendix A.1. Theoretical Description of the NMR Second Moment

NMR second moments in a rigid lattice of a solid-state material with a well-known molecular and crystal structure can be calculated using the van Vleck formula. In a powdered sample, the van Vleck formula can be represented for like spins and unlike spins as follows [39,40]:

$$M_{2,\text{rigid}}^{II} = \frac{3}{5}\gamma_I^2\hbar^2 I(I+1)\frac{1}{N_I}\sum_{j,k}^{N_I} r_{j,k}^{-6}, \tag{A1a}$$

$$M_{2,\text{rigid}}^{IS} = \frac{4}{15}\gamma_S^2\hbar^2 S(S+1)\frac{1}{N_S}\sum_{j,m}^{N_S} r_{j,m}^{-6}, \tag{A1b}$$

where I and S are the spins of NMR-active nuclei, γ_I and γ_S are the gyromagnetic ratios of nuclear spins I and S, respectively, $r_{j,k}$ and $r_{j,m}$ are internuclear distances, and N_I and N_S are the number of I and S spins, respectively. In this study, ^{1}H ($I = 1/2$) is the observed resonant nucleus. The NMR second moments for the observed nucleus are given as a sum of the respective contributions from the like spins and the unlike spins:

$$M_{2,\text{rigid}}^{I} = M_{2,\text{rigid}}^{II} + \sum_{S} M_{2,\text{rigid}}^{IS}. \tag{A2}$$

Here, we take into account three kinds of nucleus as unlike spins, namely ^{19}F ($S = 1/2$), ^{10}B ($S = 3$), and ^{11}B ($S = 3/2$).

When molecules that include the observed nuclei move, the NMR second moments are lowered in a manner that depends on their motional modes. If the internuclear vector undergoes isotropic rotation, such as a molecule in an isotropic liquid, the second moment in the rigid lattice is completely averaged out to zero ($M_{2,ave}^{I} = 0$). This situation corresponds to the isotropic reorientation of BF_4^- in the ELM-11 crystal. When the molecular motion is anisotropic (for example, by rotation about one

axis), the second moment in the rigid lattice is partially averaged out. In this case, the anisotropy parameter, q^2, which represents the degree of the motion anisotropy, is defined as follows:
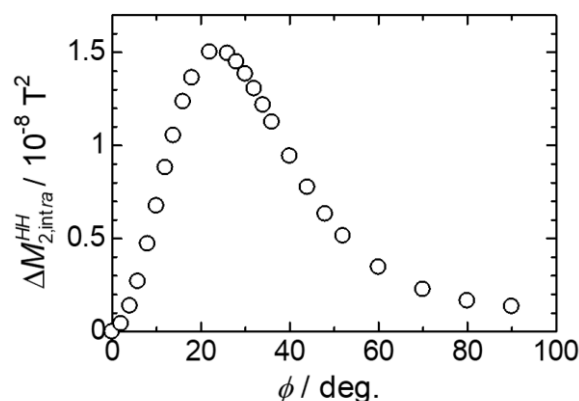
$$q^2 = (M^I_{2,rigid} - M^I_{2,ave})/M^I_{2,rigid'} \tag{A3}$$

where $M^I_{2,ave}$ is the second moment after motional averaging. Using the reduction in the second moment, $\Delta M^I_2 = M^I_{2,rigid} - M^I_{2,ave}$ and $\Delta M^I_2 = q^2 M^I_{2,rigid'}$ q^2 is determined by the nature of the molecular motion. When the internuclear vector jumps at a flip angle ϕ while maintaining angle θ with respect to a fixed axis, q^2 is given by [40,41]:

$$q^2 = \frac{3}{4}\left(\sin^2 2\theta \sin^2 \frac{\phi}{2} + \sin^4 \theta \sin^2 \phi\right). \tag{A4}$$

Using Equations (A1)–(A4), we calculated the ^{1}H and ^{19}F second moments in the rigid lattices for the three crystal structures of ELM-11, as well as the reductions in the second moments when BF_4^- isotropically reorients and when the 4,4′-bipyridine linkers flip. The second moments in the rigid lattices determined for the ^{1}H and ^{19}F nuclei are summarized in Tables A1 and A2 in Appendix A.

The reduction in the second moment due to intramolecular ^{1}H-^{1}H magnetic dipolar interactions, $\Delta M^{HH}_{2,\ intra'}$ was evaluated using Equation (A4) using the ideal 4,4′-bipyridine molecular structure when the pyridine ring flips around the C–C axis. Figure A1 shows the $\Delta M^{HH}_{2,\ intra}$ value as a function of the flip angle. The $\Delta M^{HH}_{2,\ intra}$ value increases with increasing flip angle to a maximum at 22°, and then decreases gradually. The torsion angle of the 4,4′-bipyridine unit is 54.6° in **1** and 70.64° in **2**. When the ring flips with these torsion angles, the $\Delta M^{HH}_{2,\ intra}$ value is expected to be $(0.2–0.4) \times 10^{-8}$ T^2. In contrast, the torsion angles are 14.98° and 17.52° in **3**, and ring flipping with these torsion angles is expected to give $\Delta M^{HH}_{2,\ intra}$ values of $(1–1.3) \times 10^{-8}$ T^2.

Figure A1. Reduction in the ^{1}H second moment due to intramolecular ^{1}H-^{1}H dipolar interactions in the 4,4′-bipyridine moiety.

Appendix A.2. ^{1}H Second Moments

Table A1. ^{1}H second moments (in 10^{-8} T^2) for all ELM-11 substances.

Interaction	Rigid Lattice	Averaged Value		
		bpy Flip	BF$_4^-$ Rotation	bpy Flip + BF$_4^-$ Rotation
1				
bpy 1 (0.09°)[1]				
$M_{2,intra}^{HH}$	7.348	7.348	7.348	7.348
$M_{2,inter}^{HH}$	2.865	1.327	2.865	1.327
$M_{2,inter}^{HF}$	1.217	1.217	0.692	0.692
total	11.43	9.892	10.905	9.367
bpy 2 (54.6°)[1]				
$M_{2,intra}^{HH}$	2.086	1.634	2.086	1.634
$M_{2,inter}^{HH}$	2.829	2.264	2.829	2.264
$M_{2,inter}^{HF}$	0.883	0.443	0.499	0.317
total	5.798	4.341	5.414	4.215
2				
bpy 1 (0.74°) [1]				
$M_{2,intra}^{HH}$	5.683	5.683	5.683	5.683
$M_{2,inter}^{HH}$	1.267	1.252	1.267	1.252
$M_{2,inter}^{HF}$	1.301	1.301	0.637	0.637
total	8.251	8.236	7.587	7.572
bpy 2 (70.64°)[1]				
$M_{2,intra}^{HH}$	1.958	1.735	1.958	1.735
$M_{2,inter}^{HH}$	1.278	1.152	1.278	1.152
$M_{2,inter}^{HF}$	0.808	0.435	0.576	0.250
total	4.044	3.322	3.812	3.137
3				
bpy 1 (0.52°) [1]				
$M_{2,intra}^{HH}$	8.454	8.454	8.454	8.454
$M_{2,inter}^{HH}$	0.664	0.572	0.664	0.572
$M_{2,inter}^{HF}$	0.712	0.712	0.370	0.370
total	9.830	9.738	9.488	9.396
bpy 2 (14.98°) [1]				
$M_{2,intra}^{HH}$	6.202	5.045	6.202	5.045
$M_{2,inter}^{HH}$	0.690	0.670	0.690	0.670
$M_{2,inter}^{HF}$	0.612	0.612	0.368	0.368
total	7.504	6.327	7.260	6.083
bpy 1′ (17.52°) [1]				
$M_{2,intra}^{HH}$	6.093	4.756	6.093	4.756
$M_{2,inter}^{HH}$	0.725	0.540	0.725	0.540
$M_{2,inter}^{HF}$	0.682	0.682	0.373	0.373
total	7.500	5.978	7.191	5.669
bpy 2′ (49.46°) [1]				
$M_{2,intra}^{HH}$	2.357	1.770	2.357	1.770
$M_{2,inter}^{HH}$	0.586	0.319	0.586	0.319
$M_{2,inter}^{HF}$	0.507	0.146	0.299	0.079
total	3.450	2.235	3.242	2.168

[1] The number in parentheses is the torsion angle of the 4,4′-bipyridine linker around C-C axis.

Appendix A.3. ^{19}F *Second Moment Values*

Table A2. ^{19}F second moments (in 10^{-8} T^2) for all ELM-11 substances.

Interaction	Rigid Lattice	Averaged Value		
		bpy Flip	BF$_4^-$ Rotation	bpy Flip + BF$_4^-$ Rotation
1				
$M_{2,intra}^{FF}$	6.507	6.507	0	0
$M_{2,inter}^{FF}$	6.872	6.872	2.369	2.369
$M_{2,inter}^{FH}$	5.337	4.220	3.028	2.563
$M_{2,intra}^{F10B}$	0.757	0.757	0	0
$M_{2,intra}^{F11B}$	8.660	8.660	0	0
total	28.133	27.016	5.397	4.932
2				
$M_{2,intra}^{FF}$	6.337	6.337	0	0
$M_{2,inter}^{FF}$	6.485	6.485	0.089	0.089
$M_{2,inter}^{FH}$	5.358	5.088	3.080	2.622
$M_{2,intra}^{F10B}$	0.729	0.729	0	0
$M_{2,intra}^{F11B}$	8.343	8.343	0	0
total	27.252	26.982	3.169	2.711
3				
$M_{2,intra}^{FF}$	5.478	5.478	0	0
$M_{2,inter}^{FF}$	2.811	2.811	0.040	0.040
$M_{2,inter}^{FH}$	6.302	2.486	3.537	1.308
$M_{2,intra}^{F10B}$	0.628	0.628	0	0
$M_{2,intra}^{F11B}$	7.189	7.189	0	0
total	22.408	18.592	3.577	1.348

Appendix B. Theoretical Background for NMR Spin-Lattice Relaxation of Multi-Spins

There are four kinds of NMR active nucleus in ELM-11, namely ^{1}H ($I = 1/2$), ^{19}F ($S = 1/2$), ^{10}B ($S = 3$), and ^{11}B ($S = 3/2$). In such a multi-spin system, fluctuations in the magnetic dipolar interactions between like and unlike spins causes magnetic relaxation between spin systems and the lattice. In particular, the ^{1}H and ^{19}F nuclei, which have relatively large gyromagnetic ratios, have large magnetic dipolar interactions with other spins. In such a case, the effect of cross relaxation, which involves relaxation through other spins, in addition to the direct relaxation from each spin system to the lattice, cannot be ignored. The effect of cross relaxation imparts non-exponential behavior on the recovery of both ^{1}H and ^{19}F magnetizations. In ELM-11, the ^{1}H and ^{19}F nuclei are regarded to contribute to cross relaxation because ^{1}H-^{10}B and ^{1}H-^{11}B magnetic dipolar interactions are much smaller than ^{1}H-^{19}F magnetic dipolar interactions. However, since the ^{19}F-^{10}B and ^{19}F-^{11}B magnetic dipolar interactions are somewhat larger than the ^{1}H-^{1}H and ^{1}H-^{19}F dipolar interactions, the interactions between ^{19}F and ^{10,11}B are treated as contributing to the ^{19}F relaxation rate.

Now, in such a system, the recovery rate of the magnetization of different spins obeys the following differential equation [40]:

$$\frac{d\boldsymbol{M}}{dt} = -\boldsymbol{R}(\boldsymbol{M} - \boldsymbol{M}_\infty), \tag{A5}$$

where ${}^t\boldsymbol{M} = [M^H, M^F]$ and $\boldsymbol{M}_\infty = [M_\infty^H, M_\infty^F]$. The relaxation rates actually observed are R' and R'', which are the eigenvalues of the relaxation matrix, $\boldsymbol{R}$. For simplicity, we assume the following form of $\boldsymbol{R}$ in this study:

$$\boldsymbol{R} = \begin{bmatrix} R_{HH} & R_{HF} \\ R_{FH} & R_{FF} \end{bmatrix}. \tag{A6}$$

Diagonalization of matrix $\boldsymbol{R}$ leads to the following eigenvalues [14,15,23]:

$$R' = \frac{1}{2}(R_{HH} + R_{FF}) + \frac{1}{2}\left[(R_{HH} + R_{FF})^2 - 4R_{HH}R_{FF} + 4R_{HF}R_{FH}\right]^{1/2}, \tag{A7a}$$

$$R'' = \frac{1}{2}(R_{HH} + R_{FF}) - \frac{1}{2}\left[(R_{HH} + R_{FF})^2 - 4R_{HH}R_{FF} + 4R_{HF}R_{FH}\right]^{1/2}. \tag{A7b}$$

If the magnitudes of the off-diagonal elements means that they cannot be ignored, then cross relaxation needs to be taken into account. In that case, the ^{1}H and ^{19}F magnetizations are expected to recover non-exponentially. The diagonal and off-diagonal elements in matrix $\boldsymbol{R}$ represent the spin-lattice relaxation rates caused by fluctuations in the magnetic dipolar interactions between the like- and unlike-spins as follow [40]:

$$R_{ii} = \frac{2}{3}\gamma_i^2 \Delta M_2^{ii} g_1(\omega_i, \tau_i) + \frac{1}{2}\gamma_i^2 \sum_j \Delta M_2^{ij} g_2(\omega_i, \omega_j, \tau_i), \tag{A8a}$$

$$R_{ij} = \frac{1}{2}\gamma_j^2 \Delta M_2^{ji}(N_j/N_i) g_3(\omega_i, \omega_j, \tau_i). \tag{A8b}$$

Here, we ignore the contribution of the cooperative motion between BF_4^- and 4,4′-bipyridine ($1/\tau_c = p/\tau_H + (1-p)/\tau_F; 0 < p < 1$). The analytical formulas for $g_1(\omega_i, \tau_i)$, $g_2(\omega_i, \omega_j, \tau_i)$, and $g_3(\omega_i, \omega_j, \tau_i)$ are given by [11,14,15,21,23]:

$$g_1(\omega_i, \tau_i) = \frac{\tau_i}{1 + \omega_i^2\tau_i^2} + \frac{4\tau_i}{1 + 4\omega_i^2\tau_i^2}, \tag{A9a}$$

$$g_2(\omega_i, \omega_j, \tau_i) = \frac{\tau_i}{1 + (\omega_i - \omega_j)^2\tau_i^2} + \frac{3\tau_i}{1 + \omega_i^2\tau_i^2} + \frac{6\tau_i}{1 + (\omega_i + \omega_j)^2\tau_i^2}, \tag{A9b}$$

$$g_3(\omega_i, \omega_j, \tau_i) = \frac{-\tau_i}{1 + (\omega_i - \omega_j)^2\tau_i^2} + \frac{6\tau_i}{1 + (\omega_i + \omega_j)^2\tau_i^2}. \tag{A9c}$$

Assuming a thermal activation process for the fluctuation of the internuclear vector, the temperature dependence of τ_i (i = H, F) is given by the Arrhenius equation:

$$\tau_i = \tau_{0,i} \exp(E_{a,i}/RT), \tag{A10}$$

where $E_{a,i}$ (i = H, F) is the activation energy for BF_4^- and 4,4′-bipyridine.

　　The reductions in the second moment, ΔM_2^{ii} and ΔM_2^{ij}, can be calculated from the crystal structure by assuming the appropriate motional mode. In this study, we evaluated ΔM_2^{ii} and ΔM_2^{ij} for the isotropic reorientation of BF_4^- and the torsional flipping of 4,4′-bipyridine around the C–C axis. However, we treat ΔM_2^{ii} and ΔM_2^{ij} as variables during actual data analysis and then optimize the above equations to fit the experimental T_1 data. As a result, the validity of the motional mode is discussed by comparing the ΔM_2^{ii} and ΔM_2^{ij} values obtained with the calculated ones.

　　Moreover, in a multinuclear spin system containing both ^{1}H and ^{19}F nuclei, the nuclei relax with relaxation rates R' and R'', which are the eigenvalues of the relaxation matrix $\boldsymbol{R}$. As a result, both magnetizations recover non-exponentially. However, in the case of the closed form of ELM-11, the ^{1}H magnetization recovered exponentially, as shown in Figure A2. In multinuclear spin systems containing both ^{1}H and ^{19}F nuclei, the magnetization recovery curves exhibit single exponential

behavior in some limiting cases. The first occurs when the contributions of the cross-relaxation rates R_{FH} and R_{HF} are much smaller than R_{HH} and R_{FF} (R_{HH}, R_{FF} >> R_{FH}, R_{HF}), while the other involves the ^{1}H nuclei relaxing significantly faster than the other nuclei (R_{HH} >> R_{FF}, R_{FH}, R_{HF}). In this case, $1/T_{1HH} \approx R_{HH}$ and $1/T_{1FF} \approx R_{FF}$ [50–52]. In particular, when the contribution from like spins dominate, the following well-known formula for the spin-lattice relaxation rate is obtained:

$$1/T_{1HH} = \frac{2}{3}\gamma_H^2 \Delta M_2^{HH} \left[\frac{\tau_H}{1 + \omega_H^2 \tau_H^2} + \frac{4\tau_H}{1 + 4\omega_H^2 \tau_H^2} \right]. \tag{A11}$$

In the closed form of ELM-11, assuming that the T_1 value (520 µs) below 250 K is dominated by R_{1p}, the contribution of R_{1d} at the T_1 minimum is determined to be 1.1×10^{-2} s^{-1}, and the ΔM_2^H value that gives rise to this T_1 minimum value is determined to be 25.4×10^{-8} T^2 using Equation (A11). While this is a relatively reasonable value, the expected value of the second moment reduced by feasible thermal motion in ELM-11, which averages the ^{1}H-^{1}H and ^{1}H-^{19}F dipolar interactions, is ~2×10^{-8} T^2 (see Table 1). This is only 1/10 of 25.4×10^{-8} T^2 and therefore, cannot explain the experimental value well.

Other case is: R_{HH}, $R_{FF} \approx R_{FH}$, R_{HF}, in which one of the two eigenvalues is almost zero; hence, the observed relaxation rate becomes [51]:

$$1/T_{1HH} = 1/T_{1FF} = R_{HH} + R_{FF}, \tag{A12}$$

where R_{HH} and R_{FF} are diagonal elements of the relaxation matrix **R**, which are given by Equations (A7)−(A9). In this case, the fluctuations in the ^{19}F-^{19}F, ^{19}F-^{1}H, and ^{19}F-^{10,11}B magnetic dipolar interactions, in addition to the ^{1}H-^{1}H and ^{1}H-^{19}F pairs, also contribute to relaxation. In particular, the isotropic reorientation of BF$_4^-$ is expected to reduce the second moment of the ^{19}F nuclei by 22.7×10^{-8} T^2 (see Table 2), which is sufficiently large to explain the observed T_1 minimum value. Therefore, this situation seems to be appropriate for ELM-11.
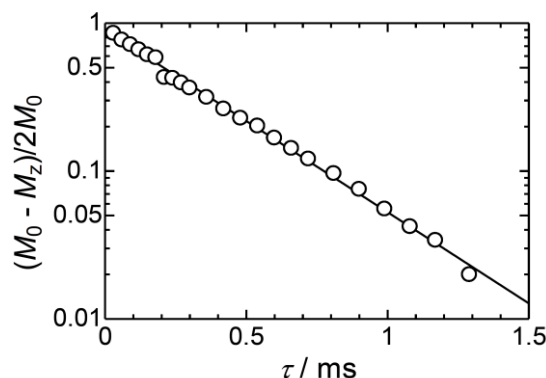
Figure A2. ^{1}H magnetization recovery curve at 233 K for the closed form of ELM-11 determined by the inversion-recovery method.

References

1. Kitagawa, S.; Kitaura, R.; Noro, S. Functional porous coordination polymers. *Angew. Chem. Int. Ed.* **2004**, *43*, 2334–2375. [CrossRef] [PubMed]
2. Fletcher, A.J.; Thomas, K.M.; Rosseinsky, M.J. Flexibility in metal-organic framework materials: Impact on sorption properties. *J. Solid State Chem.* **2005**, *178*, 2491–2510. [CrossRef]
3. Férey, G. Hybrid porous solids: Past, present, future. *Chem. Soc. Rev.* **2008**, *37*, 191–214. [CrossRef] [PubMed]
4. Li, D.; Kaneko, K. Hydrogen bond-regulated microporous nature of copper complex-assembled microcrystals. *Chem. Phys. Lett.* **2001**, *335*, 50–56. [CrossRef]

5.   Kitagawa, S.; Matsuda, R. Chemistry of coordination space of porous coordination polymers. *Coord. Chem. Rev.* **2007**, *251*, 2490–2509. [CrossRef]

6.   Tanaka, D.; Nakagawa, K.; Higuchi, M.; Horike, S.; Kubota, Y.; Kobayashi, T.C.; Takata, M.; Kitagawa, S. Kinetic gate-opening process in a flexible porous coordination polymer. *Angew. Chem. Int. Ed.* **2008**, *47*, 3914–3918. [CrossRef] [PubMed]

7.   Serre, C.; Millange, F.; Thouvenot, C.; Noguès, M.; Marsolier, G.; Louër, D.; Férey, G. Very large breathing effect in the first nanoporous chromium (III)-based solids: MIL-53 or $Cr^{III}(OH) \cdot \{O_2C\text{-}C_6H_4\text{-}CO_2\} \cdot \{HO_2C\text{-}C_6H_4\text{-}CO_2H\}_x \cdot H_2O_y$. *J. Am. Chem. Soc.* **2002**, *124*, 13519–13526. [CrossRef] [PubMed]

8.   Coudert, F.-X.; Jeffroy, M.; Fuchs, A.H.; Boutin, A.; Mellot-Draznieks, C. Thermodynamics of guest-induced structural transitions in hybrid organic-inorganic frameworks. *J. Am. Chem. Soc.* **2008**, *130*, 14294–14302. [CrossRef]

9.   Mason, J.A.; Oktawiec, J.; Taylor, M.K.; Hudson, M.R.; Rodriguez, J.; Bachman, J.E.; Gonzalez, M.I.; Cervellino, A.; Guagliardi, A.; Brown, C.M.; et al. Methane storage in flexible metal–organic frameworks with intrinsic thermal management. *Nature* **2015**, *527*, 357–361. [CrossRef]

10.   Krause, S.; Bon, V.; Senkovska, I.; Stoeck, U.; Wallacher, D.; Többens, D.M.; Zander, S.; Pillai, R.S.; Maurin, G.; Coudert, F.X.; et al. A pressure-amplifying framework material with negative gas adsorption transitions. *Nature* **2016**, *532*, 348–352. [CrossRef]

11.   Tanaka, H.; Hiraide, S.; Kondo, A.; Miyahara, M.T. Modeling and visualization of CO_2 adsorption on elastic layer-structured metal−organic framework-11: Toward a better understanding of gate adsorption behavior. *J. Phys. Chem. C* **2015**, *119*, 11533–11543. [CrossRef]

12.   Hiraide, S.; Tanaka, H.; Miyahara, M.T. Understanding gate adsorption behaviour of CO_2 on elastic layer-structured metal–organic framework-11. *Dalton Trans.* **2016**, *45*, 4193–4202. [CrossRef] [PubMed]

13.   Yang, J.; Yu, Q.; Zhao, Q.; Liang, J.; Dong, J.; Li, J. Adsorption CO_2, CH_4 and N_2 on two different spacing flexible layer MOFs. *Micropor. Mesopor. Mater.* **2012**, *161*, 154–159. [CrossRef]

14.   Bon, V.; Senkovska, I.; Wallacher, D.; Heerwig, A.; Klein, N.; Zizak, I.; Feyerherm, R.; Dudzik, E.; Kaskel, S. In situ monitoring of structural changes during the adsorption on flexible porous coordination polymers by X-ray powder diffraction: Instrumentation and experimental results. *Micropor. Mesopor. Mater.* **2014**, *188*, 190–195. [CrossRef]

15.   Kondo, A.; Kojima, N.; Kajiro, H.; Noguchi, H.; Hattori, Y.; Okino, F.; Maeda, K.; Ohba, T.; Kaneko, K.; Kanoh, H. Gas adsorption mechanism and kinetics of an elastic layer-structured metal−organic framework. *J. Phys. Chem. C* **2012**, *116*, 4157–4162. [CrossRef]

16.   Bousquet, B.; Coudert, F.-X.; Fossati, A.G.J.; Neimark, A.V.; Fuchs, A.H.; Boutin, A. Adsorption induced transitions in soft porous crystals: An osmotic potential approach to multistability and intermediate structures. *J. Chem. Phys.* **2013**, *138*, 174706. [CrossRef]

17.   Watanabe, S.; Sugiyama, H.; Adachi, H.; Tanaka, H.; Miyahara, M.T. Free energy analysis for adsorption-induced lattice transition of flexible coordination framework. *J. Chem. Phys.* **2009**, *130*, 164707. [CrossRef]

18.   Numaguchi, R.; Tanaka, H.; Watanabe, S.; Miyahara, M.T. Simulation study for adsorption-induced structural transition in stacked-layer porous coordination polymers: Equilibrium and hysteretic adsorption behaviors. *J. Chem. Phys.* **2013**, *138*, 054708. [CrossRef] [PubMed]

19.   Kitaura, R.; Fujimoto, K.; Noro, S.; Kondo, M.; Kitagawa, S. A pillared-layer coordination polymer network displaying hysteretic sorption: $[Cu_2(pzdc)_2(dpyg)]_n$ (pzdc = pyrazine-2,3-dicarboxylate; dpyg = 1,2-di(4-pyridyl)-glycol). *Angew. Chem. Int. Ed.* **2002**, *41*, 133–135. [CrossRef]

20.   Kitaura, R.; Seki, K.; Akiyama, G.; Kitagawa, S. Porous coordination-polymer crystals with gated channels specific for supercritical gases. *Angew. Chem. Int. Ed.* **2003**, *42*, 428–431. [CrossRef]

21.   Seo, J.; Matsuda, R.; Sakamoto, H.; Bonneau, C.; Kitagawa, S. A Pillared-layer coordination polymer with a rotatable pillar acting as a molecular gate for guest molecules. *J. Am. Chem. Soc.* **2009**, *131*, 12792–12800. [CrossRef] [PubMed]

22.   Uemura, K.; Yamasaki, Y.; Komagawa, Y.; Tanaka, K.; Kita, H. Two-step adsorption/desorption on a jungle-gym-type porous coordination polymer. *Angew. Chem. Int. Ed.* **2007**, *46*, 6662–6665. [CrossRef] [PubMed]

23. Hye, J.C.; Dinca, M.; Long, J.R. Broadly hysteretic H_2 adsorption in the microporous metal-organic framework Co(1,4-benzenedipyrazolate). *J. Am. Chem. Soc.* **2008**, *130*, 7848–7850.

24. Kondo, A.; Noguchi, H.; Ohnishi, S.; Kajiro, H.; Tohdoh, A.; Hattori, Y.; Xu, W.C.; Tanaka, H.; Kanoh, H.; Kaneko, K. Novel Expansion/shrinkage modulation of 2D layered MOF triggered by clathrate formation with CO_2 molecules. *Nano Lett.* **2006**, *6*, 2581–2584. [CrossRef] [PubMed]

25. Kondo, A.; Noguchi, H.; Carlucci, L.; Proserpio, D.M.; Ciani, G.; Kajiro, H.; Ohba, T.; Kanoh, H.; Kaneko, K. Double-step gas sorption of a two−dimensional metal−organic framework. *J. Am. Chem. Soc.* **2007**, *129*, 12362–12363. [CrossRef] [PubMed]

26. Kanoh, H.; Kondo, A.; Noguchi, H.; Kajiro, H.; Tohdoh, A.; Hattori, Y.; Xu, W.C.; Inoue, M.; Sugiura, T.; Morita, K.; et al. Elastic layer-structured metal organic frameworks (ELMs). *J. Colloid Interface Sci.* **2009**, *334*, 1–7. [CrossRef] [PubMed]

27. Cheng, Y.; Kajiro, H.; Noguchi, H.; Kondo, A.; Ohba, T.; Hattori, Y.; Kaneko, K.; Kanoh, H. Tuning of gate opening of an elastic layered structure MOF in CO_2 sorption with a trace of alcohol molecules. *Langmuir* **2011**, *27*, 6905–6909. [CrossRef]

28. Ichikawa, M.; Kondo, A.; Noguchi, H.; Kojima, N.; Ohba, T.; Kajiro, H.; Hattori, Y.; Kanoh, H. Double-step gate phenomenon in CO_2 sorption of an elastic layer-structured MOF. *Langmuir* **2016**, *32*, 9722–9726. [CrossRef]

29. Hiraide, S.; Tanaka, H.; Ishikawa, N.; Miyahara, M.T. Intrinsic thermal management capabilities of flexible metal−organic frameworks for carbon dioxide separation and capture. *ACS Appl. Mater. Interfaces* **2017**, *9*, 41066–41077. [CrossRef]

30. Kultaeva, A.; Bon, V.; Weiss, M.S.; Pöppl, A.; Kaskel, S. Elucidating the formation and transformation mechanisms of the switchable metal−organic framework ELM-11 by powder and single-crystal EPR study. *Inorg. Chem.* **2018**, *57*, 11920–11929. [CrossRef]

31. Jiang, Y.; Huang, J.; Kasumaj, B.; Jeschke, G.; Hunger, M.; Mallat, T.; Baiker, A. Adsorption-desorption induced structural changes of Cu-MOF evidenced by solid state NMR and EPR spectroscopy. *J. Am. Chem. Soc.* **2009**, *131*, 2058–2059. [CrossRef] [PubMed]

32. Panich, A.M.; Sergeev, N.A. Towards determination of distances between nanoparticles and grafted paramagnetic ions by NMR relaxation. *Appl. Magn. Reson.* **2018**, *49*, 195–208. [CrossRef] [PubMed]

33. Kristinaityte, K.; Zalewski, T.; Kempka, M.; Sakirzanovas, S.; Baziulyte-Paulaviciene, D.; Jurga, S.; Rotomskis, R.; Valeviciene, N.R. Spin–lattice relaxation and diffusion processes in aqueous solutions of gadolinium-based upconverting nanoparticles at different magnetic fields. *Appl. Magn. Reson.* **2019**, *50*, 553–561. [CrossRef]

34. Yamabayashi, T.; Atzori, M.; Tesi, L.; Cosquer, G.; Santanni, F.; Boulon, M.-E.; Morra, E.; Benci, S.; Torre, R.; Chiesa, M.; et al. Scaling up electronic spin qubits into a three-dimensional metal−organic framework. *J. Am. Chem. Soc.* **2018**, *140*, 12090–12101. [CrossRef]

35. Bokor, M.; Marek, T.; Tompa, K. Solid-state NMR of 1-propyltetrazole complexes of iron(II) and zinc(II). 1. [1]H spin–lattice relaxation time. *J. Magn. Reson. A* **1996**, *122*, 157–164. [CrossRef]

36. Lim, A.R. Tetragonal-orthorhombic-tetragonal phase transitions in organic-inorganic perovskite-type $(CH_3NH_3)_2MnCl_4$. *Solid State Commun.* **2017**, *267*, 18–22.

37. Jang, S.E.; Kim, M.J.; Lim, A.R. Structural geometry of the layered perovskite-type (CH3CH2CH2NH3)2CuCl4 single crystal near phase transition temperatures. *AIP Adv.* **2018**, *8*, 105324. [CrossRef]

38. Lim, A.R.; Kim, S.H. Study on paramagnetic interactions of $(CH_3NH_3)_2CoBr_4$ hybrid perovskites based on nuclear magnetic resonance (NMR) relaxation time. *Molecules* **2019**, *24*, 2895. [CrossRef]

39. Abragam, A. *The Principles of Nuclear Magnetism*; Oxford University Press: New York, NY, USA, 1961.

40. Mikuli, E.; Hetmańczyk, J.; Grad, B.; Kozak, A.; Wąsicki, J.W.; Bilski, P.; Hołderna-Natkaniec, K.; Medycki, W. The relationship between reorientational molecular motions and phase transitions in $[Mg(H_2O)_6](BF_4)_2$, studied with the use of ^{1}H and ^{19}F NMR and FT-MIR. *J. Chem. Phys.* **2015**, *142*, 064507. [CrossRef]

41. Soda, G.; Chihara, H. Note on the theory of nuclear spin relaxation exact formulae in the weak collision limit. *J. Phys. Soc. Jpn.* **1974**, *36*, 954–958. [CrossRef]

42. Wąsicki, J.; Pająk, Z.; Kozak, A. Cation and anion reorientation at phase transition in pyridinium tetrafluoroborate. *Z. Naturforsch.* **1990**, *45a*, 33–36. [CrossRef]

43. Mikuli, E.; Hetmańczyk, Ł.; Medycki, W.; Kowalska, A. Phase transitions and molecular motions in $[Zn(NH_3)_4](BF_4)_2$ studied by nuclear magnetic resonance, infrared and Raman spectroscopy. *J. Phys. Chem. Solids* **2007**, *68*, 96–103. [CrossRef]

44. Mikuli, E.; Grad, B.; Medycki, W.; Hołderna-Natkaniec, K. Phase transitions and molecular motions in $[Cd(H_2O)_6](BF_4)_2$ studied by DSC, ^1H and ^{19}F NMR and FT-MIR. *J. Solid State Chem.* **2004**, *177*, 3795–3804. [CrossRef]

45. Pérez-Jiménez, Á.J.; Sancho-García, J.C.; Pérez-Jordá, J.M. Torsional potential of 4,4′-bipyridine: Ab initio analysis of dispersion and vibrational effects. *J. Chem. Phys.* **2005**, *123*, 134309. [CrossRef] [PubMed]

46. Emsley, J.W.; Stephenson, D.S.; Lindon, J.C.; Lunazzi, L.; Pulga, S. Structure and conformation of 4,4′-bipyridyl by nuclear magnetic resonance spectroscopy of a nematic solution. *J. Chem. Soc. Perkin Trans. 2* **1975**, 1541–1544. [CrossRef]

47. Lowe, I.J.; Tse, D. Nuclear spin-lattice relaxation via paramagnetic centers. *Phys. Rev.* **1968**, *166*, 279–291. [CrossRef]

48. Lee, C.E.; Choi, I.; Kim, J.E.; Lee, C.H. Nuclear magnetic relaxation in dense paramagnet $CuF_2 \cdot 2H_2O$. *J. Phys. Soc. Jpn.* **1994**, *63*, 3509–3514. [CrossRef]

49. Bloembergen, N. On the interaction of nuclear spins in a crystalline lattice. *Physica* **1949**, *15*, 386–426. [CrossRef]

50. Albert, S.; Gutowsky, H.S. Nuclear relaxation and spin exchange in ammonium hexafluorophosphate (NH_4PF_6). *J. Chem. Phys.* **1973**, *59*, 3585–3594. [CrossRef]

51. Blinc, R.; Lahajnar, G. Magnetic resonance study of molecular motion in cubic $(NH_4)_2SiF_6$. *J. Chem. Phys.* **1967**, *47*, 4146–4152. [CrossRef]

52. Zdanowska-Frączek, M.; Medycki, W. ^1H NMR study of $N(CH_3)_4H(ClF_2CCOO)_2$. *Solid State Nucl. Magn. Reson.* **2000**, *15*, 189–193. [CrossRef]

53. Satterlee, J.D. Fundamental concepts of NMR in paramagnetic systems. Part II: Relaxation effects. *Concepts Magn. Reson.* **1990**, *2*, 119–129. [CrossRef]

54. Moreau, F.; Kolokolov, D.I.; Stepanov, A.G.; Easun, T.L.; Dailly, A.; Lewis, W.; Blake, A.J.; Nowell, H.; Lennox, M.J.; Besley, E.; et al. Tailoring porosity and rotational dynamics in a series of octacarboxylate metal-organic frameworks. *Proc. Natl. Acad. Sci. USA* **2017**, *114*, 3056–3061. [CrossRef] [PubMed]

55. Inukai, M.; Fukushima, T.; Hijikata, Y.; Ogiwara, N.; Horike, S.; Kitagawa, S. Control of molecular rotor rotational frequencies in porous coordination polymers using a solid-solution approach. *J. Am. Chem. Soc.* **2015**, *137*, 12183–12186. [CrossRef]

56. Takemura, H.; Nakashima, S.; Kon, N.; Yasutake, M.; Shinmyozu, T.; Inazu, T. A study of C-F···M$^+$ interaction: Metal complexes of fluorine-containing cage compounds. *J. Am. Chem. Soc.* **2001**, *123*, 9293–9298. [CrossRef] [PubMed]